

ORIGINAL ARTICLE

Open Access



Dynamic Analysis and Parametric Optimization of Telescopic Tubular Mast Applied on Solar Sail

Chenyang Ji^{1,2,3}, Jinguo Liu^{1,2*}, Chenchen Wu^{1,2}, Pengyuan Zhao^{1,2,4} and Keli Chen^{1,2}

Abstract

Large-scale solar sails can provide power to spacecraft for deep space exploration. A new type of telescopic tubular mast (TTM) driven by a bistable carbon fiber-reinforced polymer tube was designed in this study to solve the problem of contact between the sail membrane and the spacecraft under light pressure. Compared with the traditional TTM, it has a small size, light weight, high extension ratio, and simple structure. The anti-blossoming and self-unlocking structure of the proposed TTM was described. We aimed to simplify the TTM with a complex structure into a beam model with equal linear mass density, and the simulation results showed good consistency. The dynamic equation was derived based on the equivalent model, and the effects of different factors on the vibration characteristics of the TTM were analyzed. The performance parameters were optimized based on a multiobjective genetic algorithm, and prototype production and load experiments were conducted. The results show that the advantages of the new TTM can complete the deployment of large-scale solar sails, which is valuable for future deep space exploration.

Keywords Telescopic tubular mast, Solar sail, Genetic algorithm, Modal analysis, Optimization

1 Introduction

Solar sails are most likely to be used in deep space exploration in the future, and the area of the solar sail must be sufficiently large to achieve adequate thrust. When the size of the solar sail is very large, the displacement of the sail membrane under solar pressure will increase [1, 2]. The solar sail must be kept from the spacecraft using the deployment mechanisms to minimize damage caused by the sail membrane contacting the spacecraft [3, 4].

Many space deployable structures have been developed, including hinged truss extension arms, thin-walled tubular extension arms, inflatable extension arms, and tension integration system extension arms [5–7]. Many researchers have conducted related research on thin-walled tubular extension arms, including structural parameter optimization, environmental coupling analysis, and material blossoming. Yildiz et al. [8] used a particle swarm intelligence algorithm to optimize the size and prestress of the extension arm of a tension structure. Yang et al. [9] optimized the stretching and winding process of a C-section thin-walled composite stretch arm and obtained the best design parameter values for the stretch arm using the NLPQL algorithm. Bai et al. [10, 11] conducted a thermal and winding analysis of the lenticular composite extension arm in a simulated space environment. Jordan conducted experiments on the traction device of a lenticular extension arm, achieving the extension and contraction of the lenticular extension arm and preventing blossoming [12]. Ding et al. [13] designed

*Correspondence:

Jinguo Liu

liujinguo@sia.cn

¹ State Key Laboratory of Robotics, Shenyang Institute of Automation, Chinese Academy of Science, Shenyang 110016, China

² Institutes for Robotics and Intelligent Manufacturing, Chinese Academy of Sciences, Shenyang 110169, China

³ School of Mechanical Engineering and Automation, Northeastern University, Shenyang 110819, China

⁴ University of Chinese Academy of Sciences, Beijing 100049, China

and analyzed the winding device of rope-driven space deployable structures. Soykasap et al. [14] researched composite hinges and ribbon springs for extending arms [15–17]. Furthermore, scholars have shown interest in origami technology for extension arms [18, 19]. Different extension arms have their advantages and disadvantages. The stability and high strength of the extension arms are critical to the successful completion of the mission during interstellar voyages. Among extension arms, the space extension arm can be used as the support structure of the solar sail owing to its advantages, such as high precision, high strength, and high reliability. Therefore, it is necessary to analyze its dynamic characteristics and conduct parameterized design and optimization.

The TTM was first applied to the Dornier system in Germany. Its deployment length can reach 25 m, and it is used as a military communication facility. Joachim et al. developed a lenticular ultralight extension arm that can be used in space missions, such as solar sails, and conducted zero-gravity experiments [20]. Michael designed a windable truss mast for solar sails, whose length could reach 100–1000 m [21]. Christoph et al. [22, 23] designed and experimented with the carbon fiber-reinforced polymer (CFRP) extension arm used on the solar sail and proposed improvements for future missions. Johnson et al. [24] summarized and prospected NASA's research on solar sails. In addition to the application on solar sails, TTMs can be applied to the extension mechanism of off-orbit sails. Craig et al. [25] used inflatable masts to support off-orbit sails to complete the off-orbit mission, and the satellite reentered the atmosphere after 72 days. Juan et al. [26] designed and developed the off-orbit sails for low earth orbit and conducted full-scale deployment and impact tests. Wei et al. [27] analyzed the inflatable arms and membrane folds of the inflatable deployable solar sail. Mark et al. [28–30] conducted related research on inflatable extension arms.

Compared with the traditional space extension arm, the TTM driven by the bistable CFRP tube designed in this study achieved the goals of small volume, light weight, large extension ratio, a simple and reliable structure through structural innovation, and the application of composite materials. In this method, the TTM with a complex structure is assumed to be equivalent to a beam model with an equal linear mass density. The equivalent model results show consistency and reduce the workload involved in simulation engineering. The Euler–Bernoulli beam model is established based on the equivalent model to analyze the effects of different factors on the vibration characteristics of the TTM. The particularity of the rocket transportation process is established, the effects of six working conditions on the natural frequency of the TTM are analyzed, and the fixing method with the

highest natural frequency is selected. The difference with the traditional single-objective optimization method is that the multiobjective genetic optimization algorithm can simultaneously achieve the relative optimum within a specific range when optimizing the performance parameters of the TTM. The objective function can be increased or decreased based on the demand, which is significant for the rapid design and selection of the space extension arm and the reduction of the design cycle.

The summary of each section of this paper is as follows. The design of the stretching unit and driving structure of the TTM is presented in Section 2. In Section 3, the Euler–Bernoulli continuous beam theory is used to establish the dynamic model of the TTM. In addition, the convergence of the Euler–Bernoulli beam and the segmental model of the TTM for the equivalent model is analyzed, and the modal analysis results are compared using ABAQUS. In Section 4, the vibration characteristics under different working conditions are analyzed. Six factors, including the material, diameter, wall thickness, and the number of sections, are selected to analyze their effects on the vibration characteristics, and sensitivity analysis is presented. In Section 5, the multiobjective genetic algorithm is used to optimize the natural frequency, mass, bending rigidity, and extension ratio of the TTM. The deployment experiments with tip-load are described. The conclusion is summarized in Section 6.

2 Structure Design of TTM

The TTM mainly comprises two parts: the stretching unit and the driving structure. The main structure is shown in Figure 1, which mainly includes the bistable CFRP tube, motor, reel, stretching unit, and roller. The motor is fixed by a flange and drives the reel. The bistable carbon fiber is stretched out under the drive of the motor. The roller prevents the carbon fiber from blossoming, and the reel stores the bistable carbon fiber. The stretching unit is extended step by step under the action of the driving structure to complete the deployment. The stretching units consist of thin-walled tubes of the same length, and the wall thickness is generally thin to reduce the mass. The tube relies on the internal pin to complete the locking, improving the rigidity and load capacity. The outer arm of the tube is provided with a guide groove, and the

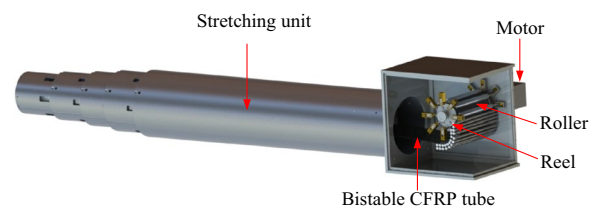


Figure 1 Main structure of each part of TTM

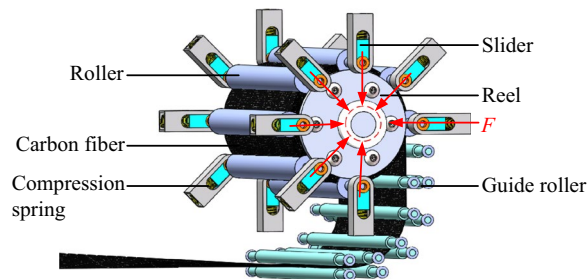


Figure 2 Drive and antiblossoming structure

guide rail is matched with the groove to prevent circumferential rotation and damage to the internal structure.

The power to extend the tube is provided by the drive mechanism. The motor drives the reel to extend the bistable carbon fiber, and the top is connected to the tube. As shown in Figure 2, multiple rollers are used to compress the bistable carbon fiber circumferentially to prevent the blossoming of the carbon fiber. The two ends of the circumferentially distributed roller are placed in the bearings inside the slider to roll smoothly and minimize friction with the carbon fiber. The bottom end of the slider can accommodate a compression spring of a specific length, and the other end of the compression spring is in contact with the sidewall. It should be noted that the compression spring length should be slightly extended to ensure that the bistable carbon fiber on the reel can still provide sufficient radial force to prevent blossoming, as shown in Figure 2.

Figure 3 shows a schematic of the locking–unlocking process of the pin. When locked, the pin is pressed into the pinhole by the spring to complete the lock. When unlocked, the unlocking structure pulls the pin out of the hole under the CFRP tube tension to complete the unlocking.

Compared with the traditional space deployable structures, applying a new structure and bistable CFRP tube will significantly reduce the weight of the TTM, simplify the structure, and considerably increase the success rate of space missions. In addition, the thickness of the carbon fiber tube is small, which can reduce the tube length and achieve light weight and a super large extension ratio without increasing the volume of the collapsed state.

3 Dynamic Analysis of TTM

The additional load at the top of the TTM is the solar sail. As shown in Figure 4, the solar sail can provide power for spacecraft that perform interstellar missions, save fuel, reduce the launch load, and carry additional equipment. Solar sails rely on solar pressure to achieve thrusting.

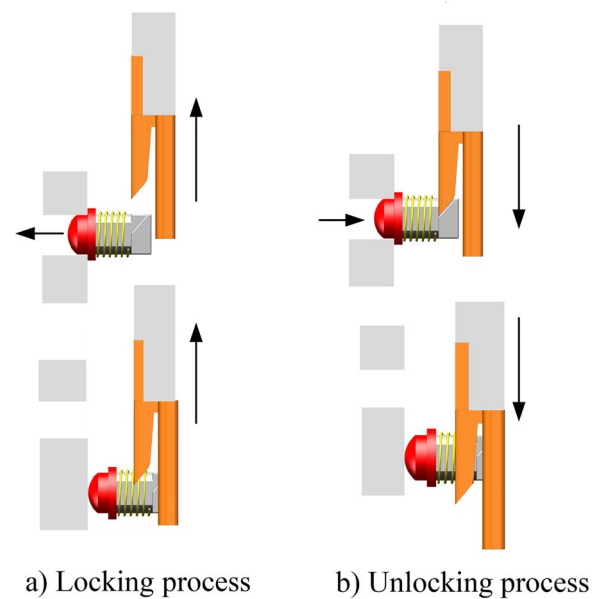


Figure 3 Pin lock and unlock process

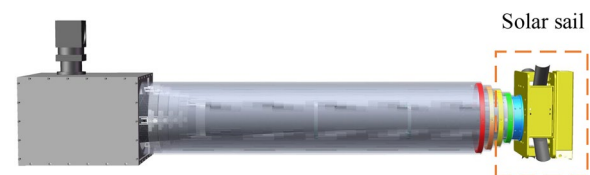


Figure 4 Solar sail load at tip of TTM



Figure 5 Workflow of TTM and solar sail

The solar sail is placed on top of the TTM and reaches the designated orbit for deployment. The TTM keeps the solar sail away from the spacecraft to prevent the sail membrane from affecting the spacecraft or causing damage to the sail membrane in contact with the spacecraft. The work process is shown in Figure 5. The TTM is deployed step by step under the motor drive. When the TTM is deployed to the maximum length, the top solar sail starts working until it is fully deployed.

Many complex parts exist in the TTM. In addition to the tube and the mounting ring, the TTM also contains smaller parts, such as pins and springs. If the model can be simplified in the finite element simulation analysis, it can significantly minimize the workload in the analysis process, improve efficiency, and save computing resources. After the TTM is deployed, it can be regarded as a continuum structure with uniform mass distribution, which satisfies the assumptions of a perfectly elastic body and small deformation. Therefore, we propose to equate a TTM with a complex structure to a simple beam with the same linear mass density and establish its dynamic model. The equivalent beam microelement section is shown in Figure 6.

Based on the D'Alembert principle, the lateral force balance equation of the equivalent beam microelement section can be derived as expressed by Eq. (1):

$$Q(x, t) + q(x, t)dx - \left(Q(x, t) + \frac{\partial Q}{\partial x} dx \right) - \rho A(x) \frac{\partial^2 y}{\partial t^2} dx = 0. \quad (1)$$

After sorting Eq. (1), Eq. (2) is derived:

$$M + \frac{\partial M}{\partial x} dx - M - Qdx - \left[q(x, t)dx - \rho A(x) \frac{\partial^2 y}{\partial t^2} dx \right] \frac{dx}{2} = 0. \quad (2)$$

Combined with the relevant parameters, Eq. (3) can be derived:

$$f_1 = \frac{1.875^2}{2\pi} \sqrt{\frac{ED^4(1 - \alpha^4)}{64\rho(D^2 - d^2)l^4}}, \quad (3)$$

where q is the uniform load, Q is the shear force, M is the bending moment, D is the outer diameter, d is the inner diameter, l is the length, and α is the ratio of the inner diameter to the outer diameter.

3.1 TTM Equivalent Model

In this section, the finite element model in the storage state was established using ABAQUS, as shown in Figure 7(a), and the equivalent model in the deployed state is

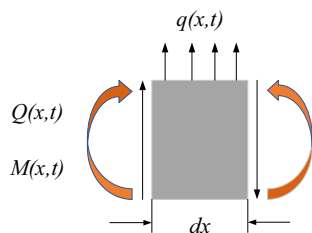


Figure 6 Model of equivalent beam microelement segment

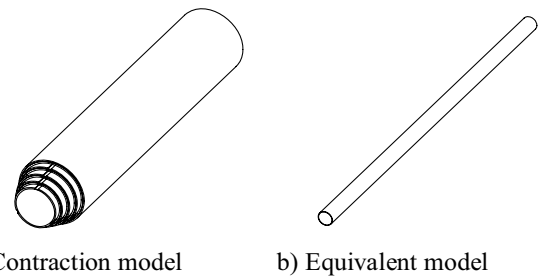


Figure 7 Model of TTM contraction and extension state: **a** Contraction model; **b** Equivalent model

shown in Figure 7(b). The mesh convergence analysis was performed to improve the calculation speed. The grid size was uniformly selected from 5–50 mm; the drawing is shown in Figure 8, where the abscissa is the reciprocal of the grid size, and the ordinate is the natural frequency in the corresponding grid size. When the grid is less than or equal to 10 mm, the natural frequency is stable (Figure 8).

3.2 Equivalent Model Verification and Modal Analysis

A segmented model and an equivalent model of the TTM were established in ABAQUS to verify the accuracy of the equivalent model. The selected mesh size of the finite element model was 10 mm, and the material was 7075 aluminum alloy.

As shown in Figures 9 and 10, that is, the formations of the segmented and equivalent models, respectively, the modes of the two models are consistent.

The frequencies of each order of the two models are listed in Table 1. The 1, 3, and 5 order frequencies are consistent, and the errors with the segmented model are 25.1%, 4.3%, and – 3.5%, respectively. The higher-order

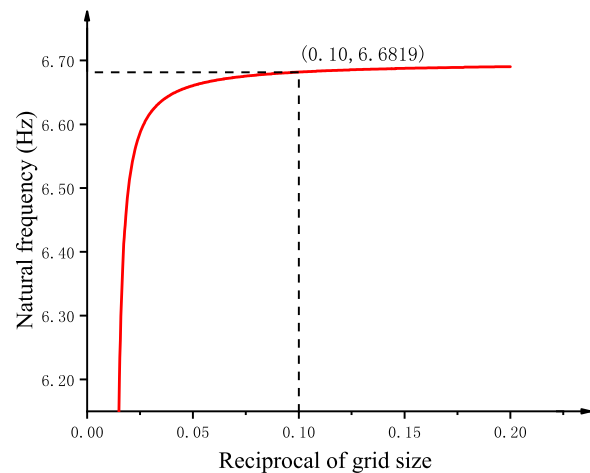


Figure 8 Mesh size convergence analysis

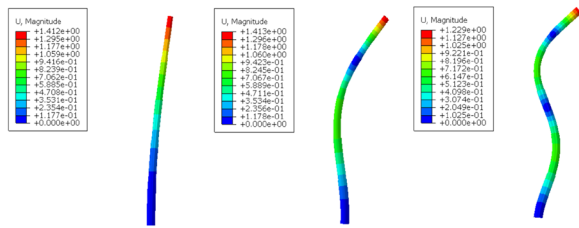


Figure 9 Modal shape of segmented model of TTM

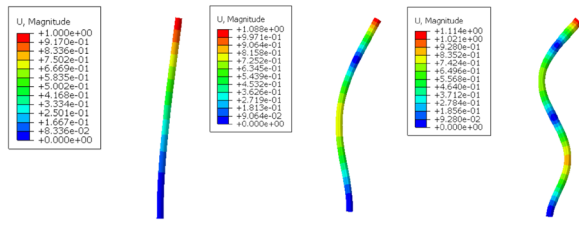


Figure 10 Modal shape of equivalent model of TTM

Table 1 Frequency of each step of TTM (Hz)

Model	1	3	5	7
Segmented model	8.92	43.15	109.46	194.27
Equivalent model	6.68	41.26	113.32	147.21

Table 2 Parameters of solar sail

Length (mm)	Width (mm)	Height (mm)	Weight (kg)	Expanded area (m ²)
100	100	49.3	1.1	0.53

errors are relatively small, satisfying the preliminary design requirements.

4 Effects of Different Factors on Vibration Characteristics

4.1 Fixing Method and Load

To reveal the effects of different working conditions, such as the fixing method during transportation, and the effects of factors, such as the wall thickness, on the

performance of TTM, we analyzed them to select the best option. The performance parameters of the solar sail are listed in Table 2.

There are two approaches to fixing the TTM during transportation: fixing at the bottom end and both ends. In the extension state, it can also be divided into two cases based on the load. Different fixing methods have a specific influence on the rigidity of the structure. The analysis models are established according to different fixing methods, and the natural frequency is extracted and analyzed. In addition, when the solar sail is fixed on the top as a load, it will affect the vibration characteristics of the TTM. We divided the fixing methods of the TTM during the transportation process into six cases and analyzed them separately. These six cases are listed in Table 3.

Figure 11 is the displacement cloud diagram for two conditions when the equivalent load of a solar sail is installed on the top of the TTM in the contraction state.

For these six cases, the base of the TTM was connected to the platform by bolts to keep it stable during transportation. In addition, the model was simplified before the analysis. Unnecessary, small chamfers were removed to minimize the appearance of low-quality meshes. The analysis data for the six cases were sorted out, and the results are shown in Table 4.

It can be seen from Table 4 that the natural frequency difference between A and C is relatively significant, and the highest increase reached 362.35%. The difference in the fixed method resulted in a more significant increase in the natural frequency. The simulation results for the six working conditions of the TTM show that the load influences the natural frequency. The rigidity of the overall structure did not change significantly owing to its small size and light weight, and the natural frequency decreased slightly. Based on the comprehensive analysis results, it is recommended to adopt the method of fixing at both ends for transportation; this is beneficial to eliminate lower frequency vibration and prevent structural damage caused by resonance.

4.2 Other Factors

The impact on the vibration characteristics of the TTM based on four aspects (the material, wall thickness,

Table 3 Different states and loads of TTM

Condition	A	B	C	D	E	F
Expanded state	—	—	—	—	Yes	Yes
Collapsed state	Yes	Yes	Yes	Yes	—	—
Top fixed	—	—	Yes	Yes	—	—
Bottom fixed	Yes	Yes	Yes	Yes	Yes	Yes
Load	—	Yes	—	Yes	—	Yes

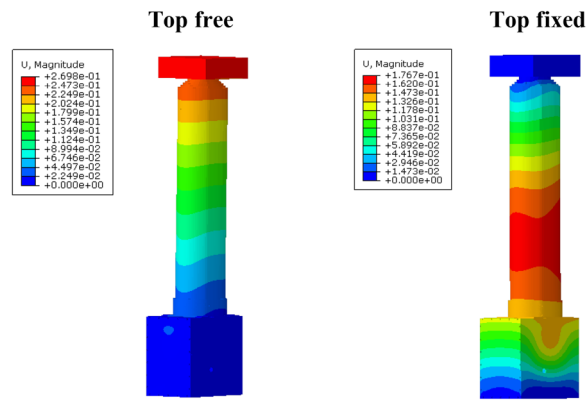


Figure 11 Displacement cloud diagram under two conditions (B/D)

diameter, and the number of sections) was investigated to further analyze the influence of different factors on the vibration characteristics of TTM. First, the influence of the material on the modal of the TTM was analyzed. Material analysis can provide support for product design. The parameters of typically used aerospace materials are listed in Table 5.

By assigning different materials to the model, the frequency information was obtained for different materials of the TTM. The frequencies in the corresponding orders of the four materials were plotted. The frequency of the TTM made of carbon fiber T700 significantly improved compared with those of other materials, and its natural frequency (the first-order frequency) increased by approximately 16.6–25.1% (Figure 12). Therefore, carbon fiber materials should be preferred in the design of TTMs. Although the 45 steel has a better natural frequency than the 7075 aluminum alloy, its high density increases transportation costs. Magnesium alloy can be replaced by aluminum alloy because of its low density and excellent vibration characteristics. Based on the comparison and analysis of the results, the carbon fiber exhibited the best overall performance, followed by the aluminum alloy, magnesium alloy, and 45 steel.

Table 5 Material characteristic parameters

Material	E (GPa)	ν	ρ (kg/m ³)	Thickness (mm)	Length (mm)
Al-7075	72	0.33	2.8×10^3	5	5320
T700	60	0.3	1.6×10^3	5	5320
Mg alloy	42.2	0.28	1.76×10^3	5	5320
45#	193	0.3	7×10^3	5	5320

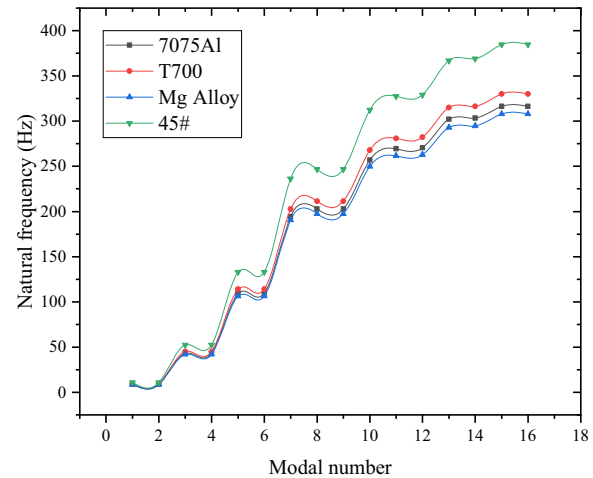


Figure 12 Effect of material on vibration characteristics

Although the wall thickness influences the TTM weight and collapsed diameter, it also influences the natural frequency. In this study, the wall thickness was used as a variable in the design, and the material was T700 carbon fiber, with a 0.5 mm gradient, to evaluate the vibration characteristics of an extension arm with a thickness of 1–5 mm.

Figure 13 is plotted according to the data obtained from the simulation. As the wall thickness gradually increases, the frequencies of each order, including the natural frequency, increase gradually. When the wall thickness is 5 mm, the high-order frequency increases significantly. Its

Table 4 Comparison of first six-order frequencies in six cases (Hz)

Mode	A	B	C	D	E	F
1	66.55	64.31	307.71	306.00	6.67	6.38
2	76.59	74.04	322.57	320.80	6.67	6.38
3	361.58	353.14	420.05	430.06	41.26	39.50
4	370.78	363.49	430.48	430.48	41.26	39.50
5	426.74	426.41	441.88	441.83	113.32	108.61
6	429.91	430.45	509.47	509.38	113.32	108.61

natural frequency is 2.84% higher than that of the 1 mm wall thickness. The relationship between weight and frequency should be considered when designing extension arms, and a smaller wall thickness should be selected to satisfy the frequency requirements.

Because of the limitation of the carrying space, the storage volume of the TTM should be as small as possible. The diameter of the TTM tube directly affects the volume; thus, it is necessary to assess the influence of diameter on the vibration characteristics. With a diameter of 180 mm as the benchmark, the effect of the diameter on the vibration characteristics was investigated with increments of 10 mm. When the wall thickness and length are constant, the natural frequency slightly increases with increasing diameter, whereas the higher-order frequency decreases (Figure 14). The diameter was selected based on the analysis results. A small diameter should be selected when the natural frequency does not change significantly. In addition, a small diameter helps to increase high-order frequencies and decrease the weight.

The extension ratio is a critical performance index of the space extension structure. The number of sections directly influences the extension ratio of the TTM. The volume of the launch vehicle is limited, and a larger extension ratio indicates a smaller storage length, making full use of the carrying space. If the length is constant, the increase in the number of sections results in an increased extension ratio. However, the number of sections should also be limited to a specific range to achieve improved performance. In this section, the length and material of the TTM remained unchanged, and the selected number of sections ranged from 3 to 7 in evaluating the influence of the number of sections on vibration. When the number of sections is 5, the natural

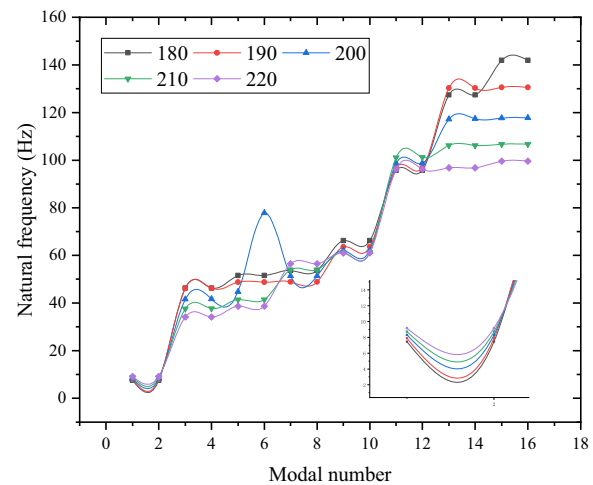


Figure 14 Effect of diameter on vibration characteristics

frequency is 2.81% higher than that of 3 sections and 3.42% lower than that of 7 sections. The results of the extension ratio are presented in Figure 15. As the number of sections increases, the natural frequency increases slightly. When the natural frequency does not change considerably, the number of sections should be selected as much as possible to obtain a larger extension ratio and excellent vibration characteristics.

4.3 Sensitivity Analysis

The sensitivity analysis was conducted using the operations research method to analyze the effects of different factors on the vibration characteristics of the TTM. The sensitivity analysis equation is expressed as follows:

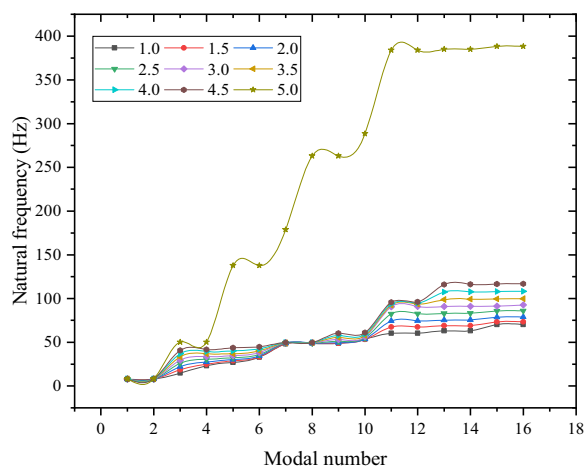


Figure 13 Effect of wall thickness on vibration characteristics

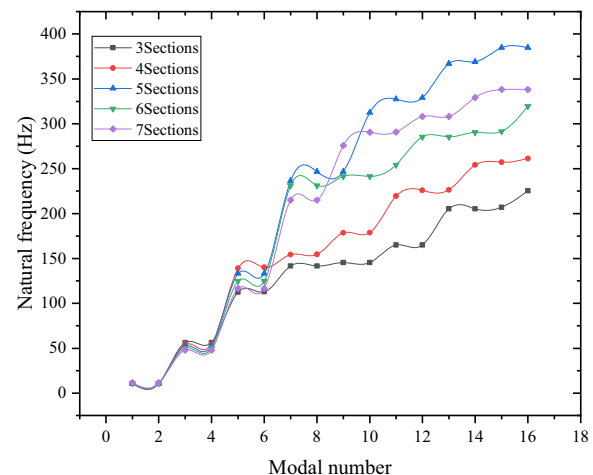


Figure 15 Effect of number of sections on vibration characteristics

$$\eta(f_i/x_j) = \lim_{\Delta x_j \rightarrow 0} \frac{(\Delta f_i/f_i)}{(\Delta x_j/x_j)}, \quad (4)$$

where f_i and x_j are not zero, Δf_i and Δx_j are the natural frequency variations and parameter variations, respectively, and x_j and f_i are structural parameters and natural frequencies under corresponding parameters, respectively. The sensitivity chart is plotted based on the simulation analysis results presented in Table 6.

It can be seen from the sensitivity analysis table that the value can be positive or negative. A positive value indicates an increase in the natural frequency, and a negative value is the opposite. The influence of diameter on the vibration characteristics is more significant than those of the number of sections and the wall thickness. Hence, the effect of diameter on the vibration characteristics should be given priority in the design. When the natural frequency must meet the task requirements, the diameter should be given priority.

5 Multiobjective Genetic Algorithm Optimization and Experimental Verification

In this section, we discuss how to obtain the optimal performance parameters of TTM using a multiobjective genetic algorithm. We then produced the prototype and conducted an experimental verification. The multiobjective genetic algorithm was proposed by Deb et al., which is based on nondominated sorting and exhibits excellent solution performance [31].

5.1 Objective Function and Feasible Range

The design of the TTM should optimize the parameters of multiple objective functions. Multiobjective optimization can be regarded as the minimum or maximum value of multiple objective functions under constraints. In general, the optimal solution of the multiobjective function is not unique, a game between variables exists, and the result is the Pareto optimal front.

The mathematical model of multiobjective function can be expressed by Eq. (5):

$$\begin{cases} \min / \max y = (f_1(x), \dots, f_n(x)), \\ x = (x_1, \dots, x_n), \end{cases} \quad (5)$$

Table 6 Sensitivity analysis under different factors

$i = j$	1	2	3	4	Average value
Wall thickness	0.0054	0.0054	0.0054	0.0117	0.0070
Diameter	1.0206	1.0223	1.0206	1.0189	1.0206
Number of sections	0.0068	0.1219	0.0566	0.1361	0.3080

where f is the objective function, x is the variable, and n is the number of variables.

Variables must be optimized within a particular feasible region. If the feasible region is not specified, extensive calculations will be required, and the parameters obtained will not satisfy actual requirements. Therefore, it is necessary to assign parameter ranges to the variables and obtain the optimal solution of the objective function for selection.

After completing the TTM design, the feasible region of the objective function is specified, and optimization is performed. The TTM is installed inside the transport rocket, and its height, radius, weight, and other parameters must be designed according to actual conditions. The extension and contraction lengths of the TTM determine its extension ratio. The extension ratio should be as high as possible to reduce the storage space. The diameter should be reasonably selected according to the overall length and working properties while ensuring sufficient strength and meeting the storage space requirements.

The objective functions to be optimized are expressed by Eq. (6):

$$\min f(x) \begin{cases} f(1) = \frac{1.875^2}{2\pi} \sqrt{\frac{EI}{\rho A l^4}}, \\ f(2) = \pi \left(\left(\frac{D}{2} \right)^2 - \left(\frac{d}{2} \right)^2 \right) l \rho, \\ f(3) = E \frac{\pi D^4 (1 - \alpha^4)}{64}, \\ f(4) = (l/x_4)/l, \end{cases} \quad (6)$$

where E is the elastic modulus of the material, ρ is the material density, I is the section moment of inertia, α is the radius ratio, D is the outer diameter of the TTM, d is the inner diameter, l is the length, and x_4 is the section number of the TTM.

Because the matrix operation is used in the optimization process, the independent variable is the column vector of x , and the variable is replaced with the sequence of x when writing the program. The objective function is the minimum value during optimization. Therefore, if the maximum value of the function is to be obtained, its reciprocal should be adopted as the objective function. The feasible ranges of the parameters are listed in Table 7.

5.2 Parameter Optimization

When the objective function and feasible region are provided, the optimization of the objective function can be conducted. Compared with traditional optimization algorithms, the random characteristics of genetic algorithms

Table 7 Feasible ranges for parameters

Variable	Feasible range
Outer diameter x_1 (m)	0.15–0.20
Wall thickness x_2 (m)	0.002–0.005
Length x_3 (m)	4.8–5.2
Number of sections x_4 (m)	5–10

Table 8 Genetic algorithm parameter settings

Parameter	Value
ParetoFraction	0.3
PopulationSize	200
MaxGeneration	300
stallGenLimit	300
TolFun	1×10^{-10}
Crossover ratio	0.8
Mutation ratio	0.2

can prevent falling into the local optimum and determine the global optimum. Traditional algorithms are generally used for solving structured problems with explicit constraints. Overall, they have the best advantage but are unsuitable for multiextreme problems. For the four objective functions in this study, multiple optimal

solutions are available in the feasible range. Hence, the multiobjective genetic algorithm can rapidly obtain the optimal solution set of the variables.

The parameters of the multiobjective genetic algorithm, including the optimal front-end individual coefficient, population size, and evolutionary algebra, were set. The related parameters are listed in Table 8.

After setting the parameters, the Gamultiobj function was used to solve the problem based on the equivalent model of the TTM, and the Pareto solution set of the multiobjective function was obtained. The results are presented in Table 9, where D is the diameter, T is the wall thickness, L is the length, N is the number of sections, F is the natural frequency, M is the mass, K is the bending rigidity, and W is the extension ratio.

The diameter tends to the given maximum value (Table 9), which means that the larger the diameter, the better the solution of the objective function. In the Pareto solution set, the length tends to the given minimum value, and the lower the value, the better the performance. The optimal solution of the number of sections is mainly at the maximum value such that the extension ratio remains unchanged during optimization. Thus, the maximum allowable number of sections can be provided at the beginning of the design.

The objective function fluctuates referred from the Pareto solution set, and a game exists among several objective function values. The parameter design should

Table 9 Multiobjective optimization Pareto solution set

D (mm)	T (mm)	L (m)	N	F (Hz)	M (kg)	K (N·m ²)	W
150.00	2.00	4.80	9.99	6.43	12.54	1.8×10^5	0.10
199.97	2.33	4.81	9.55	8.56	19.51	5.1×10^5	0.10
199.95	4.98	5.07	9.71	7.60	43.46	1.0×10^6	0.10
199.97	2.08	4.81	9.77	8.57	17.48	4.6×10^5	0.10
199.87	4.99	4.93	9.81	8.03	42.31	1.0×10^6	0.10
198.58	2.75	4.81	5.04	8.46	22.87	5.8×10^5	0.20
176.69	2.02	4.80	9.98	7.58	14.99	3.1×10^5	0.10
199.71	4.50	4.82	9.76	8.43	37.32	9.5×10^5	0.10
199.81	4.91	4.85	8.55	8.32	40.93	1.0×10^6	0.12
198.61	2.96	4.82	8.41	8.44	24.67	6.3×10^5	0.12
168.55	2.67	4.84	10.00	7.10	18.93	3.4×10^5	0.10
198.87	4.91	4.83	5.24	8.33	40.60	1.0×10^6	0.19
199.32	4.32	4.84	8.90	8.34	35.95	9.1×10^5	0.11
199.97	4.66	4.82	9.56	8.41	38.72	9.8×10^5	0.10
195.25	2.75	4.81	9.94	8.34	22.46	5.5×10^5	0.10
197.87	2.42	4.83	5.34	8.41	20.18	5.1×10^5	0.19
199.21	3.89	4.82	9.15	8.42	32.33	8.2×10^5	0.11
199.11	3.36	4.87	6.06	8.27	28.28	7.1×10^5	0.16
183.75	2.03	4.80	9.57	7.89	15.64	3.4×10^5	0.10
189.12	2.22	4.81	9.96	8.09	17.60	4.1×10^5	0.10

be selected according to the degree of importance and priority. The internal connections and changes between parameter values can be observed clearly in Figure 16.

In addition to the game phenomenon between objective functions, a process between design and target parameters exist, as shown in Figure 17. The increase in the outer diameter increases the natural frequency of the structure, which is approximately linear. In addition, it increases the bending rigidity of the structure and has a nonlinear relationship. The increase in the number of sections inevitably leads to a decrease in the extension ratio, making it possible to reduce the storage height. The increase in the wall thickness causes the bending rigidity to increase. Therefore, the bending rigidity can be significantly improved if the outer diameter and wall thickness enable change.

5.3 Repeated Deployment and Load Experiment

A proportional prototype was developed based on the data selected from the Pareto solution set, as shown in Figure 18. The entire experimental process was completed in an ultraclean laboratory.

The drive motor model selects an MD36NP51 planetary gear motor, and the rated torque can reach 2.5 N·m. The load and the TTM were connected by screws. The load of the solar sail was replaced by a cuboid of the same weight to complete the deployment experiment. The experimental process was repeated 10 times, and the deployment and repossession processes were relatively stable. In addition, experiments were performed with a load five times the weight of the solar sail, and the deployment and repossession

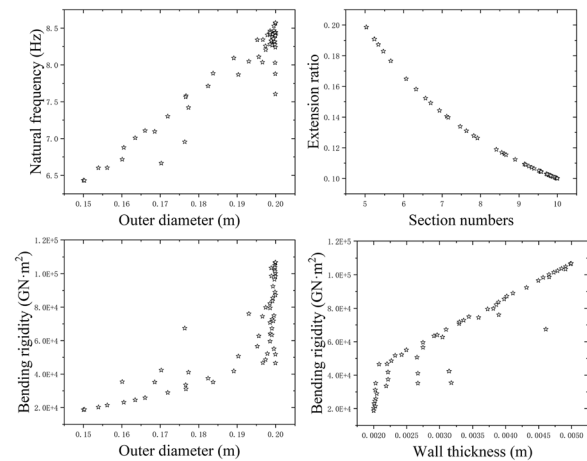


Figure 17 Game process between target and design parameters

tasks were completed, verifying the load capacity of the TTM. The entire experimental process took 12.5 s on average, and the time sequence is shown in Figure 19. In future experiments, the solar sail will be used to verify whether the unfolding process causes the vibration of the solar sail.

6 Conclusions

The main conclusions of this study are as follows.

- 1) A TTM driven by a bistable carbon fiber was designed. It has light weight, high precision, strong

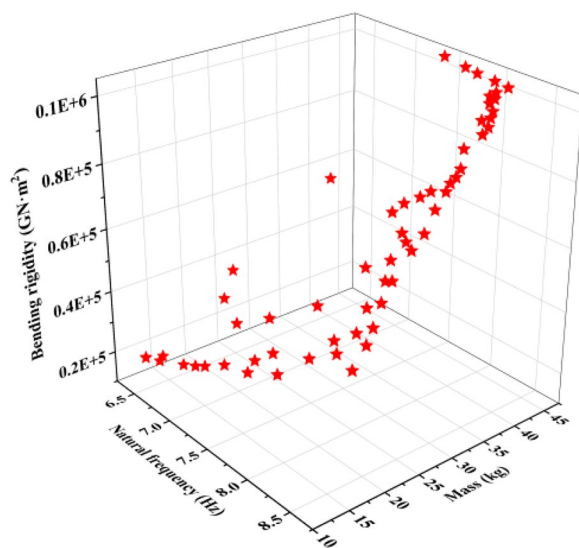


Figure 16 Pareto optimal solution of objective function

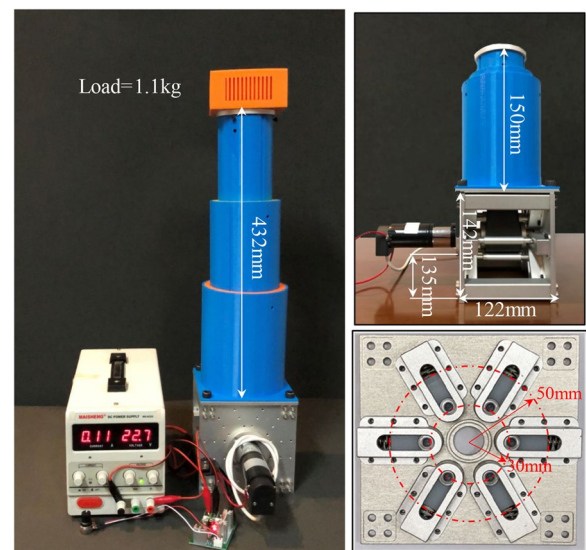


Figure 18 Prototype of TTM

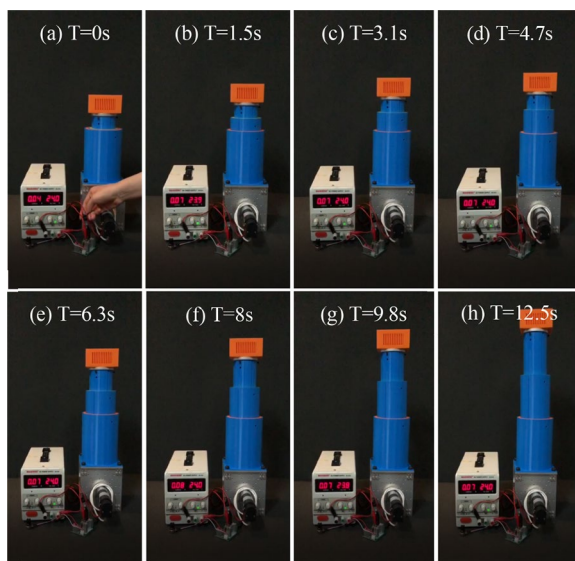


Figure 19 TTM working sequence with load

load capacity, and can be repeatedly deployed, which is essential to satisfying future space requirements.

- 2) The Euler–Bernoulli equivalent beam model and the segmented beam model were analyzed, and their natural frequency results are in good agreement.
- 3) The analysis results under different working conditions show that the performance is better when the two ends are fixed than when only one end is fixed. The influence of multiple factors, such as the wall thickness, on the vibration characteristics of the TTM, was analyzed, which has guiding significance when selecting design parameters.
- 4) The NASG-II multiobjective genetic algorithm was used to optimize the natural frequency, mass, extension ratio, and bending rigidity of the TTM, and its Pareto solution set was obtained. It is critical for the parametric design of the TTM.
- 5) The processing prototype was deployed under loading. The results show that the extension of the TTM and the repossession can be achieved smoothly.

The vibration generated during the working process is challenging to dissipate because of the unique working environment of the TTM. Therefore, vibration control will be investigated in future studies. In addition, we will attempt to increase the strength and extension ratio of the TTM and decrease the weight.

Authors' Contributions

CJ was in charge of the whole trial; CJ wrote the manuscript; JL, CW, PZ and KC assisted with sampling and laboratory analyses. All authors read and approved the final manuscript.

Authors' information

Chenyang Ji, born in 1994, is a master graduated from *Northeastern University, China*.

Jinguo Liu, born in 1978, is currently a professor and a PhD candidate supervisor at *Shenyang Institute of Automation, Chinese Academy of Science, China*.

Chenchen Wu, born in 1990, is currently an associate professor at *Shenyang Institute of Automation, Chinese Academy of Science, China*.

Pengyuan Zhao, born in 1994, is currently a PhD candidate at *State Key Laboratory of Robotics, Shenyang Institute of Automation, Chinese Academy of Science, China*.

Keli Chen, born in 1991, is currently an engineer at *Shenyang Institute of Automation, Chinese Academy of Science, China*.

Funding

Supported by National Key R&D Program of China (Grant No. 2018YFB1304600), National Natural Science Foundation of China (Grant No. 51905527), CAS Interdisciplinary Innovation Team of China (Grant No. JCTD-2018-11), State Key Laboratory of Robotics Foundation of China (Grant No. Y91Z0303).

Data availability

Data will be made available on request.

Competing interests

The authors declare no competing financial interests.

Received: 22 February 2023 Revised: 22 February 2023 Accepted: 7 March 2023

Published online: 28 March 2023

References

- [1] J G Liu, P Y Zhao, C C Wu, et al. SIASAIL-I solar sail: From system design to on-orbit demonstration mission. *Acta Astronautica*, 2022, 192: 133-142.
- [2] A A Quarta, G Mengali, L Niccolai, et al. Solar sail augmented Hohmann transfer. *IEEE Transactions on Aerospace and Electronic Systems*, 2022.
- [3] H Yang, H W Guo, Y Wang, et al. Design and experiment of triangular prism mast with tape-spring hyperelastic hinges. *Chinese Journal of Mechanical Engineering*, 2018, 31: 33.
- [4] P Y Zhao, J G Liu, C C Wu, et al. Novel surface design of deployable reflector antenna based on polar scissor structures. *Chinese Journal of Mechanical Engineering*, 2020, 33: 68.
- [5] E M Sosa, G J Thompson, E J Barbero. Experimental investigation of initial deployment of inflatable structures for sealing of rail tunnels. *Tunnelling and Underground Space Technology*, 2017, 69: 37-51.
- [6] A G Mamalis, D E Manolatos, M B Ioannidis, et al. On the response of thin-walled CFRP composite tubular components subjected to static and dynamic axial compressive loading: experimental. *Composite Structures*, 2005, 69: 407-420.
- [7] S Houliara, S A Karamanos. Buckling and post-buckling of long pressurized elastic thin-walled tubes under in-plane bending. *International Journal of Non-Linear Mechanics*, 2006, 41: 491-511.
- [8] K Yildiz, G A Lesieutre. Sizing and prestress optimization of Class-2 tensegrity structures for space boom applications. *Engineering with Computers*, 2020: 1-14.
- [9] H Yang, H Guo, R Liu, et al. Coiling and deploying dynamic optimization of a C-cross section thin-walled composite deployable boom. *Structural and Multidisciplinary Optimization*, 2019, 61: 1731-1738.
- [10] J B Bai, R A Shenoi, J J Xiong. Thermal analysis of thin-walled deployable composite boom in simulated space environment. *Composite Structures*, 2017, 173: 210-218.
- [11] J B Bai, D Chen, J J Xiong, et al. Folding analysis for thin-walled deployable composite boom. *Acta Astronautica*, 2019, 159: 622-636.
- [12] J A Firth, M R Pankow. Advanced dual-pull mechanism for deployable spacecraft booms. *Journal of Spacecraft and Rockets*, 2019, 56: 569-576.
- [13] X L Ding, H B Xiao, Q L Yang, et al. Design and analysis of a cable-winding device driving large deployable mechanisms in astrophysics missions. *Acta Astronautica*, 2020, 169: 124-137.

- [14] O Soykasap. Deployment analysis of a self-deployable composite boom. *Composite Structures*, 2009, 89: 374–381.
- [15] S J I Walker, G S Aglietti. A study of tape spring fold curvature for space deployable structures. *Proceedings of the Institution of Mechanical Engineers -- Part G*, 2007, 221: 313–325.
- [16] H M Y C Mallikarachchi, S Pellegrino. Design of ultrathin composite self-deployable booms. *Journal of Spacecraft and Rockets*, 2014, 51: 1811–1821.
- [17] Y Liu, H Du, L Liu, et al. Shape memory polymers and their composites in aerospace applications: A review. *Smart Materials & Structures*, 2014, 23: 23001–23022.
- [18] S Wu, Q Ze, J Dai, et al. Stretchable origami robotic arm with omnidirectional bending and twisting. *Proceedings of the National Academy of Sciences*, 2021, 118(36): e2110023118.
- [19] H Matsuo, H H Asada, Y Takeda. Design of a novel multiple-DOF extendable arm with rigid components inspired by a deployable origami structure. *IEEE Robotics and Automation Letters*, 2020, 5(2): 2730–2737.
- [20] J Block, M Straubel, M Wiedemann. Ultralight deployable booms for solar sails and other large gossamer structures in space. *Acta Astronautica*, 2011, 68: 984–992.
- [21] M A Brown. A deployable mast for solar sails in the range of 100–1000 m. *Advances in Space Research*, 2011, 48(11): 1747–1753.
- [22] C Sickinger, L Herbeck, E Breitbach. Structural engineering on deployable CFRP booms for a solar propelled sailcraft. *Acta Astronautica*, 2006, 58: 185–196.
- [23] P Y Zhao, J G Liu, C C Wu. Survey on research and development of on-orbit active debris removal methods. *Sci. China Tech. Sci.*, 2020, 63(11): 2188–2210.
- [24] L Johnson, R Young, E Montgomery, et al. Status of solar sail technology within NASA. *Advances in Space Research*, 2011, 48: 1687–1694.
- [25] C Underwood, A Viquerat, M Schenk, et al. InflateSail de-orbit flight demonstration results and follow-on drag-sail applications. *Acta Astronautica*, 2019, 162: 344–358.
- [26] Juan M Fernandez, Lourens Visagie, Mark Schenk, et al. Design and development of a gossamer sail system for deorbiting in low earth orbit. *Acta Astronautica*, 2014, 103: 204–225.
- [27] J Z Wei, R Q Ma, Y F Liu, et al. Modal analysis and identification of deployable membrane structures. *Acta Astronautica*, 2018, 152: 811–822.
- [28] M Schenk, A D Viquerat, K A Seffen, et al. Review of inflatable booms for deployable space structures: packing and rigidization. *Journal of Spacecraft and Rockets*, 2014, 51: 762–778.
- [29] E M Sosa, C S Wong, A Adumitroaie, et al. Finite element simulation of deployment of large-scale confined inflatable structures. *Thin-Walled Structures*, 2016, 104: 152–167.
- [30] N Katsumata, M C Natori, H Yamakawa. Analysis of dynamic behaviour of inflatable booms in zigzag and modified zigzag folding patterns. *Acta Astronautica*, 2014, 93: 45–54.
- [31] K Deb, A Pratap, S Agarwal, et al. A Fast and elitist multiobjective genetic algorithm: NSGA-II. *IEEE Transactions on Evolutionary Computation*, 2002, 6: 182–197.

Submit your manuscript to a SpringerOpen[®] journal and benefit from:

- Convenient online submission
- Rigorous peer review
- Open access: articles freely available online
- High visibility within the field
- Retaining the copyright to your article

Submit your next manuscript at ► [springeropen.com](https://www.springeropen.com)